

Article

Hybrid ZnO/MoS₂ Core/Sheath Heterostructures for Photoelectrochemical Water Splitting

Katerina Govatsi *, Aspasia Antonelou *, Labrini Sygellou, Stylianos G. Neophytides and Spyros N. Yannopoulos *

Foundation for Research and Technology, Hellas—Institute of Chemical Engineering Sciences (FORTH/ICE-HT), P.O. Box 1414, GR-26504 Rio-Patras, Greece; sygellou@iceht.forth.gr (L.S.); neoph@iceht.forth.gr (S.G.N.)

* Correspondence: kat.govatsi@iceht.forth.gr (K.G.); antonelou@iceht.forth.gr (A.A.); sny@iceht.forth.gr (S.N.Y.); Tel.: +30-2610965252 (S.N.Y.)

Abstract: The rational synthesis of semiconducting materials with enhanced photoelectrocatalytic efficiency under visible light illumination is a long-standing issue. ZnO has been systematically explored in this field, as it offers the feasibility to grow a wide range of nanocrystal morphology; however, its wide band gap precludes visible light absorption. We report on a novel method for the controlled growth of semiconductor heterostructures and, in particular, core/sheath ZnO/MoS₂ nanowire arrays and the evaluation of their photoelectrochemical efficiency in oxygen evolution reaction. ZnO nanowire arrays, with a narrow distribution of nanowire diameters, were grown on FTO substrates by chemical bath deposition. Layers of Mo metal at various thicknesses were sputtered on the nanowire surface, and the Mo layers were sulfurized at low temperature, providing in a controlled way few layers of MoS₂, in the range from one to three monolayers. The heterostructures were characterized by electron microscopy (SEM, TEM) and spectroscopy (XPS, Raman, PL). The photoelectrochemical properties of the heterostructures were found to depend on the thickness of the pre-deposited Mo film, exhibiting maximum efficiency for moderate values of Mo film thickness. Long-term stability, in relation to similar heterostructures in the literature, has been observed.

Keywords: ZnO; MoS₂; heterostructures; core/sheath; water splitting



Citation: Govatsi, K.; Antonelou, A.; Sygellou, L.; Neophytides, S.G.; Yannopoulos, S.N. Hybrid ZnO/MoS₂ Core/Sheath Heterostructures for Photoelectrochemical Water Splitting. *Appl. Nano* **2021**, *2*, 148–161. <https://doi.org/10.3390/applnano2030012>

Academic Editor: Angelo Maria Taglietti

Received: 2 June 2021
Accepted: 5 July 2021
Published: 7 July 2021

Publisher's Note: MDPI stays neutral with regard to jurisdictional claims in published maps and institutional affiliations.



Copyright: © 2021 by the authors. Licensee MDPI, Basel, Switzerland. This article is an open access article distributed under the terms and conditions of the Creative Commons Attribution (CC BY) license (<https://creativecommons.org/licenses/by/4.0/>).

1. Introduction

The quick depletion of natural resources and moderation of carbon dioxide emissions are currently pursued by developing low-cost alternatives of electricity supply using renewable energy sources, such as solar light. Photoelectrochemical (PEC) water splitting stands out as a promising way towards hydrogen production by solar energy-driven water splitting. Metal oxide semiconductors, such as TiO₂ [1–3], ZnO [4–6] and WO₃ [7,8], have traditionally been employed as anodes in PEC cells in view of their stability and ease of morphology manipulation, especially for ZnO [9,10]. However, the wide optical bandgaps of these materials limit their light absorption only to the UV part of the solar spectrum, which prevents the efficient exploitation of solar energy in the visible region. Hematite (α-Fe₂O₃), an abundant and non-toxic material, has also been intensively explored owing to its narrow bandgap (~2.1 eV) for solar water splitting [11], which is, however, bound to several limitations, such as low absorption, short exciton lifetime and low oxygen evolution reaction kinetics. An additional narrow bandgap semiconductor, i.e., BiVO₄, has also been systematically investigated for potential use as a photoanode in solar water splitting, despite it suffers from very low electron-hole separation yield, leading to poor efficiency conversion [12].

Recently, hybrid core/sheath nanostructures consisting of a metal oxide semiconductor core (ZnO) covered by transition metal di-chalcogenides layers (MX₂, M: Mo, W, etc., and X: Se, S₂, Te) and other chalcogenides, such as ZnSe [13,14], CdS [15] and CdSe [16,17], have been explored as potential efficient PEC anode materials stimulated by visible light benefiting from a more effective separation of photo-generated charges.

Among various layered (2D) chalcogenide crystals, MoS₂ is considered a promising material because of its tunable bandgap ranging from ~1.2 eV (indirect gap) for the bulk crystal to ~1.9 eV (direct gap) for the monolayer [18–20]. MoS₂ comprises a strong in-plane covalent bonding of S–Mo–S and weak out-of-plane van der Waals interaction between S–S in neighboring layers, further exhibiting relatively high mobility [21]. According to theoretical calculations and experimental studies, MoS₂ has high catalytic performance due to the S atoms situated at the edges of the plane, being more catalytically active than the S atoms of the basal sites of the layer [22–24]. MoS₂ can be synthesized by several methods, including hydrothermal [25], chemical vapor deposition [26], mechanical or chemical exfoliation [27], liquid-phase exfoliation [28], atomic layer deposition [29], and so on. Furthermore, MoS₂ exhibits a variety of morphologies such as nanoparticles [30], nanotubes [31], nanosheets [32], flakes [33] and quantum dots [28,34].

There are few sporadic studies about the electrochemical behavior of MoS₂ towards hydrogen evolution reaction (HER) [35]. However, the performance of the material in relation to the oxygen evolution reaction (OER) has not yet been explored systematically. Contrary to HER, the OER involves a four-electrons-step oxidation process and suffers from sluggish electrode kinetics [36]. In line with experiments and theoretical calculations, the defected edge sites and vacancies in the MoS₂ can also promote the OER [34].

In this work, we attempt to investigate the OER of core/sheath ZnO/MoS₂ heterostructures synthesized by a novel route. ZnO nanowire (NW) arrays prepared on FTO/glass substrates by chemical bath deposition stand as the scaffolds onto which the few-layer MoS₂ thin films are grown. MoS₂ sheath is prepared by low-temperature sulfurization of pre-deposited ultrathin Mo films on the ZnO surface. Controlling Mo film deposition and sulfurization conditions, heterostructures with varying thickness of MoS₂ layers down to the monolayer, are prepared. Structural and morphological characterization is employed to provide information on microstructural characteristics of the heterostructures and the chemical environment of the interface between the core and sheath materials. The influence of the thickness of the sheath layer on the PEC properties of these hybrid nanostructures is explored.

2. Experimental

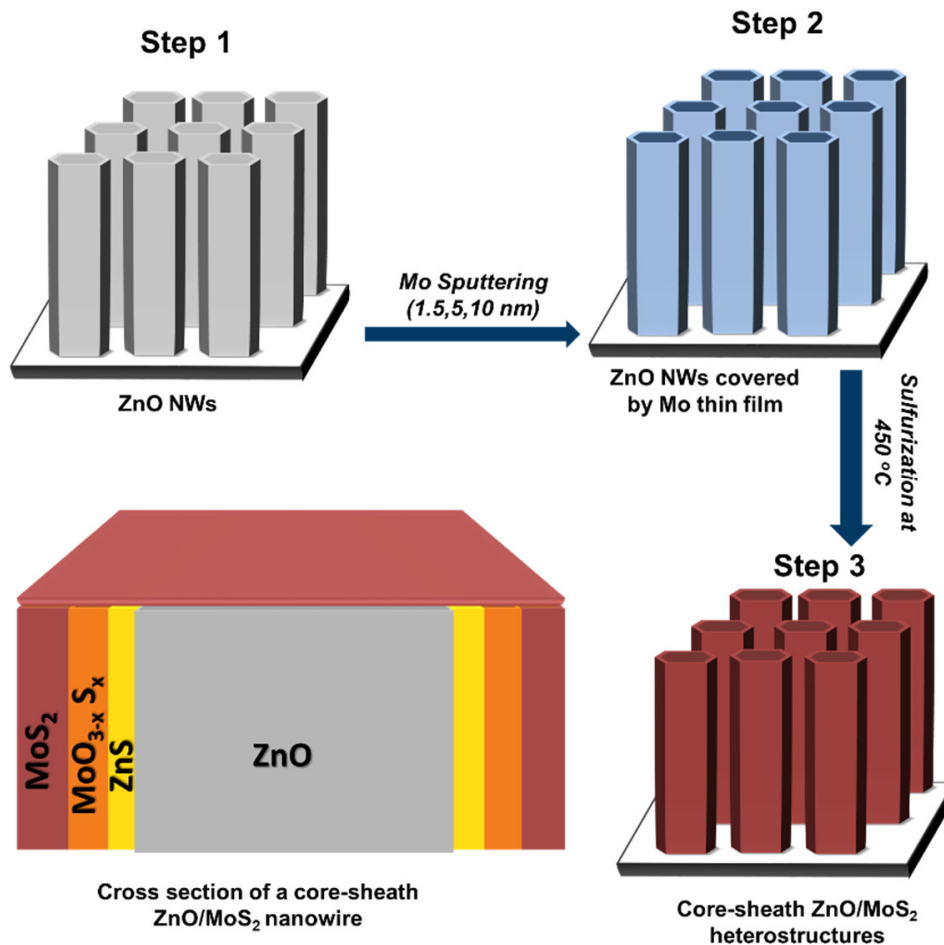
2.1. Growth of ZnO NW Arrays on FTO Substrates

The synthesis of ZnO NW arrays onto FTO/glass substrates has been described in detail elsewhere [37]. After the standard cleaning of the substrates, the method includes the dissolution of 0.05 M of zinc acetate dihydrate, ZnAc (Zn(CH₃COO)₂ · 2H₂O, Sigma-Aldrich ACS reagent, ≥98%) in absolute ethanol. The solution is spin-coated on the substrate and thermally decomposed to form the oriented nanocrystals of the ZnO seed layer. Subsequently, the growth of ZnO NW arrays takes place in an aqueous solution containing equimolar concentrations (0.035 M) of ZnAc and hexamethylenetetramine (HMTA, C₆H₁₂N₄, Sigma-Aldrich, Louis, MI, USA, ACS reagent, ≥99.0%). The growth proceeds in a closed reactor vessel at 95 °C for 5 h. After the growth step, the NW arrays are rinsed with triple distilled water and annealed at 300 °C for 2 h.

2.2. Growth of ZnO/MoS₂ Heterostructures

Mo ultrathin films of various nominal thicknesses ranging from 1.5 to 10 nm were deposited on the ZnO surface using sputtering at low vacuum (5×10^{-2} mbar). For the formation of the MoS₂ layer, the Mo-sputtered ZnO samples were placed into a triple temperature zone furnace to sulfurize the Mo films by exposing them to sulfur vapors. Specifically, sulfur powder (Alfa Aesar, 99.9999%) was placed in an alumina boat and positioned upstream in the quartz tube of the tube furnace, while the Mo-sputtered ZnO samples were placed downstream, a few cm away from the sulfur powder. The temperature was set at 450 °C for the Mo-covered ZnO NW arrays, while sulfur powder was heated at ~150–200 °C. Prior to increasing the temperature, Ar gas was purged into the reactor with a flow rate of 100 sccm for at least 60 min to remove the residual oxygen. The purging was

kept during the heating phase, so Ar played the role of the carrier gas for the sulfur species in the gaseous phase. The nominal thickness of the sputtered Mo ultrathin film was found to control the number of MoS₂ monolayers. After the heating phase (60 min), the furnace was allowed to cool down naturally until room temperature while being continuously purged by Ar gas. Scheme 1 provides a pictorial illustration of the various synthesis steps and a cross-section of the layers that comprise the final product. The MoS₂/ZnO heterostructures prepared by pre-depositing 1.5, 5 and 10 nm of Mo metal are labeled hereafter as Mo-1.5, Mo-5 and Mo-10, respectively.



Scheme 1. A schematic of the total synthesis procedure and an overview of the cross-section of the final product.

2.3. Characterization of Morphology, Structure and Optical Properties

The morphology of the ZnO/MoS₂ heterostructures was characterized using field emission scanning electron microscopy (FE-SEM, Zeiss SUPRA, 35VP-FEG) operating at 15 keV and transmission electron microscopy (TEM, JEOL JEM-2100) operating at 200 kV. The crystal structure was verified by selected area electron diffraction (SAED). ZnO/MoS₂ NWs were dispersed in alcohol and spread onto a carbon-coated copper grid (200 mesh) for the TEM analysis. The chemical composition of heterostructures and their interface were characterized with X-ray photoelectron spectroscopy (XPS) and X-ray induced Auger electron spectroscopy (XAES) in an ultrahigh vacuum chamber equipped with a SPECS Phoibos 100-1D-DLD hemispherical electron analyzer and a dual Al/Mg x-ray gun. The XP spectra were recorded with MgK α at 1253.6 eV photon energy and an analyzer pass energy of 10 eV, giving a full width at half maximum (FWHM) of 0.85 eV for the Ag3d_{5/2} line. The samples were mounted on a stainless-steel sample holder to avoid charging effects. The C1s position was at 285.0 eV due to carbon contamination. The crystallinity and thickness

of the few-layer MoS₂ were investigated via Raman spectroscopy (Jobin-Yvon, LabRam HR-800) using the excitation of 441.6 nm. A microscope objective with 50× magnification is used to focus the light onto a spot of about 3 μm in diameter. The optical properties were characterized by photoluminescence (PL) spectroscopy (Cary Eclipse Fluorescence Spectrophotometer G9800A, Agilent Technologies, Burlington, VT, USA, excitation at 500 nm) and ultraviolet-visible (UV-Vis) spectroscopy (Hitachi, U-3000).

2.4. Photoelectrochemical Measurements

The geometric area of the PEC anodes is about 2 × 2 cm², while the electrode working area illuminated and exposed to the electrolyte was ~1 cm². PEC characterization was performed using a three-electrode configuration and an AUTOLAB potentiostat (PGSTAT30 model). A Pt wire and a hydrogen reference electrode were used as counter and reference electrodes, respectively. The electrolyte was an aqueous solution of 0.24 M Na₂S 9H₂O (Sigma-Aldrich ACS reagent ≥ 98%) and 0.35 M Na₂SO₃ (Sigma-Aldrich ≥ 98%), pH 11.5, which was degassed by bubbling pure Ar for at least 30 min prior to the electrical measurements to remove dissolved gases. The light source (solar simulator) comprised a 150 W Xe arc lamp delivering an intensity of 100 mW cm⁻². The sample was illuminated from the backside (bare glass surface). The electrochemical characterization and the evaluation of the heterostructures were observed by performing linear sweep voltammetry (LSV) and cyclic voltammetry (CV) with a scan rate of 50 mV s⁻¹.

3. Results and Discussion

3.1. Electron Microscopy Analysis

Figure 1 displays the FE-SEM images of the (a) bare ZnO NRs and (b–d) the heterostructures with a different layer thickness of MoS₂ sheath; (b), (c), and (d) correspond to Mo-1.5, Mo-5 and Mo-10, respectively. The 1D rod-like ZnO structures are clearly observed in all cases. The average diameter of ZnO NWs is approximately 120 nm, while their length is ~1 μm. FE-SEM images reveal that the initially smooth surface of the ZnO NWs (a) attain a textured form due to the growth of the MoS₂ sheath. The effect becomes progressively more evident as the nominal Mo thickness increases from 1.5 to 10 nm. The formation of the sheath is apparent for all thicknesses of pre-deposited Mo films. In the case of Mo-5 nm and Mo-10, FE-SEM reveals the growth of islands, especially on the top of the rods.

The morphology and the core/sheath structure of the nanorods are further investigated by TEM and high-resolution TEM (HRTEM). Figure 2a,b show low-magnification TEM micrographs of ZnO NWs and the Mo-10 ZnO/MoS₂ heterostructure. The MoS₂ sheath is evidenced by the semitransparent film grown around the ZnO nanowire in Figure 2b. The HRTEM image in Figure 2c illustrates the interplanar distances of (002) ZnO planes, with the corresponding lattice spacing at 0.26 nm. Additionally, Figure 2d displays the interlayer arrangement of hexagonal 2H-MoS₂ with a lattice spacing of approximately 0.62 nm, corresponding to the spacing d(002) of hexagonal 2H-MoS₂. In the same area, we can spot the d(100) of MoS₂ estimated as ~0.27 nm.

3.2. XPS Analysis

XPS survey scans, shown in Figure S1, for the heterostructures show that Zn, Mo, S, C and O elements are present. The XPS spectra of the combined Mo3d-S2s window are shown in Figure 3a,b. The Mo3d peak is analyzed into two Mo3d doublets with the spin-orbit splitting of 3.2 eV and with binding energies (BE) of Mo3d_{5/2} peak at 229.2 eV assigned to 2H-MoS₂ [38] and at 232.5 eV assigned to Mo⁺⁶ chemical state of a mixed oxysulfide MoO_{3-x}S_x species [39]. The % concentration of the MoS₂ component is ~65% and ~72% for Mo-5 and Mo-10 heterostructures, respectively. Figure 3c,d show the S2p XPS peaks, which consist of S2p doublets with the spin-orbit splitting of 1.2 eV. The BE of the S2p_{3/2} peak is found at 161.9 eV and can be assigned to species related to MoS₂ and ZnS since the S2p_{3/2} peak for both components lies at nearly the same BE [38,40]. Traces of sulfur oxide are revealed by the weak peak at 168.9 eV assigned to sulphates (SO₄ anions) and/or

sulphite (SO_3 anions) species [41] Figure 3e,f display the $\text{Zn}2p_{3/2}$ spectra and the ZnLMM X-ray-induced Auger spectra, respectively. Since the literature values for the $\text{Zn} 2p_{3/2}$ BEs are quite similar for ZnS and ZnO, the Auger parameter, defined as the sum of the binding energy of the $\text{Zn} 2p_{3/2}$ and the kinetic energy of the $\text{Zn} M_{3L_{45}}L_{45}$, is an accurate parameter for the chemical state identification. The obtained value 2011.5 eV is in agreement with that reported in the literature for zinc(II) sulfide [40].

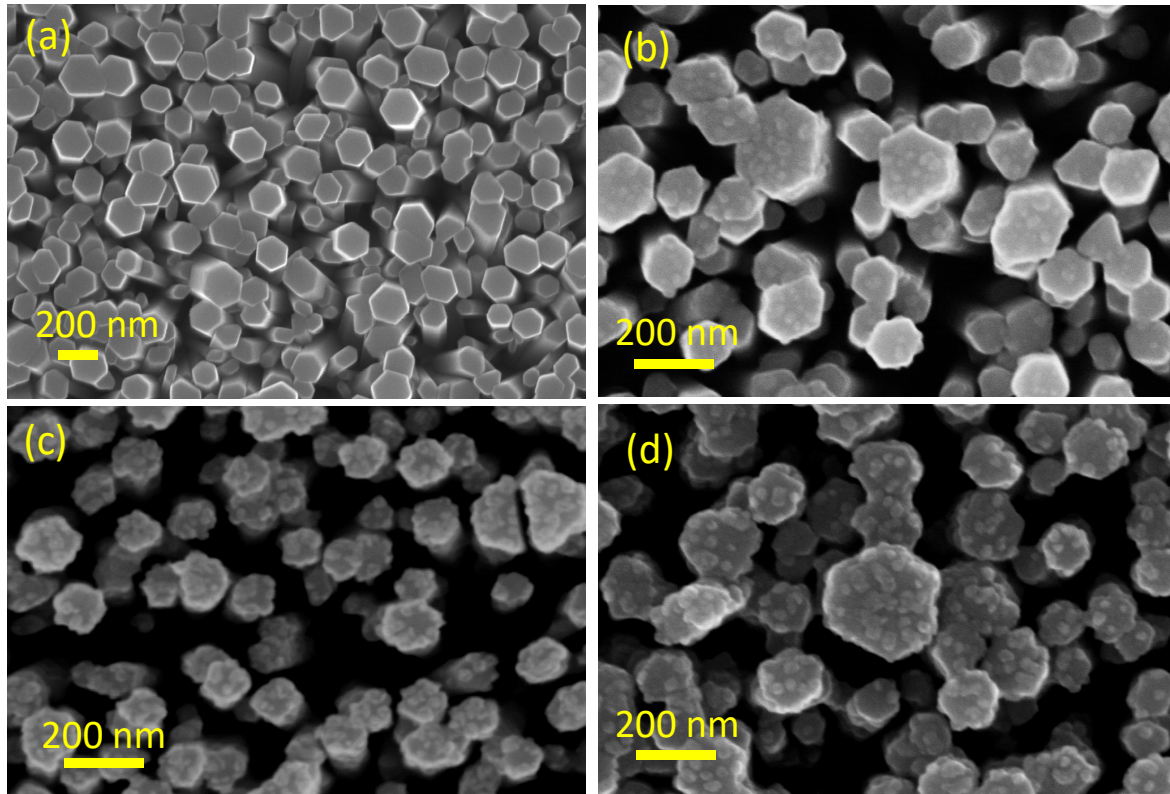


Figure 1. SEM images of (a) bare ZnO NWs. (b–d) denote ZnO/MoS₂ heterostructures with Mo nominal thickness of 1.5, 5 and 10 nm, respectively.

The relative atomic concentration of Mo, S and Zn have been derived using the Mo3d, S2p and Zn2p_{3/2} peak areas, weighted by the relative sensitivity factors and the transmission characteristics of the energy analyzer. The atomic mass ratios for the M-5 and Mo-10 heterostructures are estimated as Mo/S/Zn = 20.0/57.9/22.1 and Mo/S/Zn = 18.4/63.7/17.9, respectively. These ratios declare that the Mo/S ratio is considerably lower than the nominal value, 1/2. This finding is not unexpected given that sulfurization not only proceeds towards complete reaction with the Mo thin film, but it further takes place at a deeper level, transforming the topmost atomic layers of ZnO to ZnS and/or ZnO_yS_{1-y}. Therefore, the chemical species information furnished by XPS indicates the lack of an abrupt interface between MoS₂ and ZnO. Instead, there is a thin zone of gradual transformation between these two materials, with this zone being composed of oxy-sulfide species and possibly mixed MoO_{3-x}S_x and ZnO_yS_{1-y} species. While an abrupt interface between the two semiconductors may impose a barrier, which must be overcome by photogenerated charge carriers, the gradual variation originating from these mixed species may offer more favorable conditions for efficient charge transport and separation.

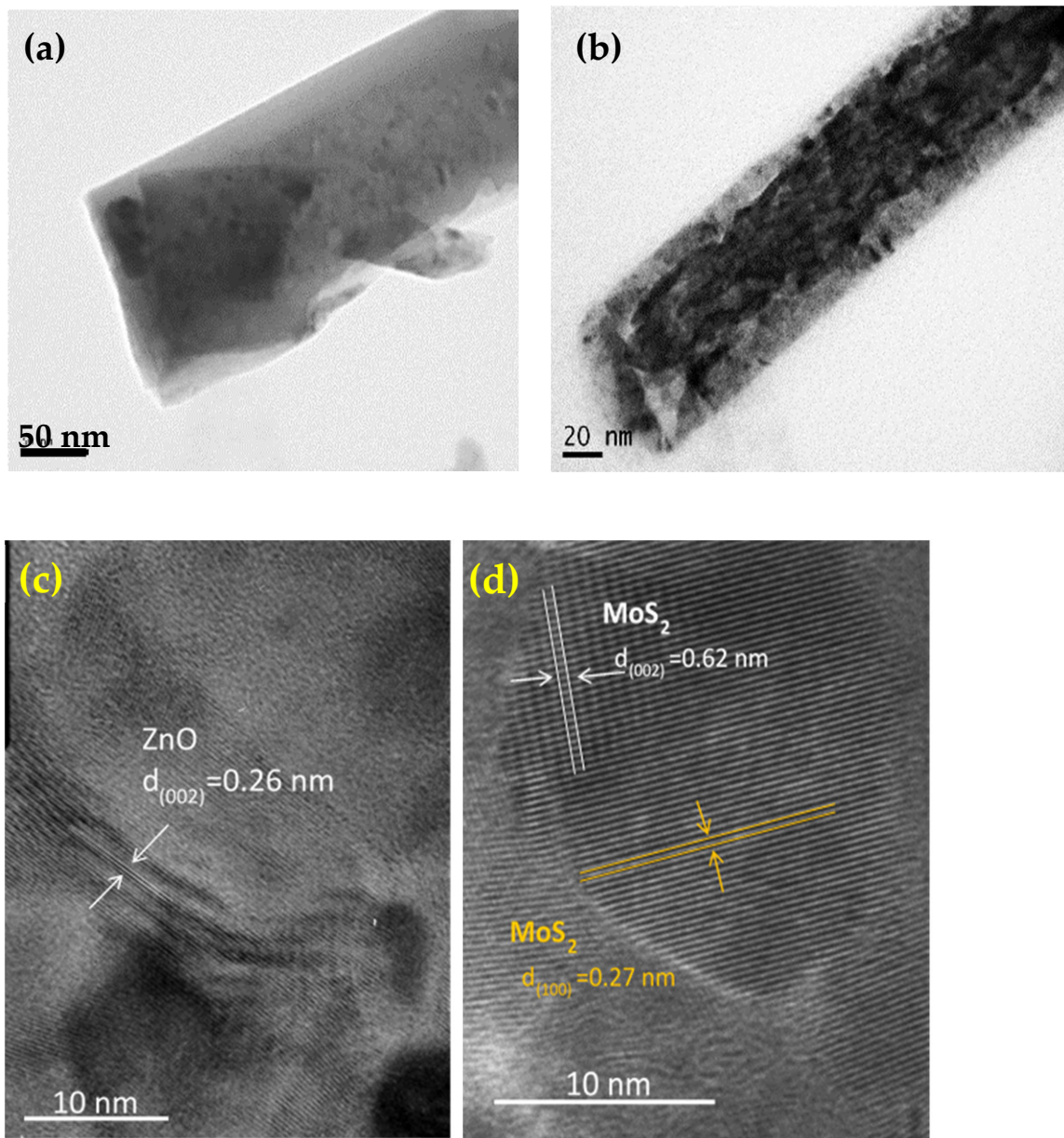


Figure 2. TEM images (a) a ZnO NW and (b) a ZnO/MoS₂ core/sheath heterostructure. HRTEM of (c) ZnO and (d) hexagonal MoS₂ showing the crystal planes (002) and (100).

3.3. Optical Properties

3.3.1. PL Spectroscopy

Optical properties of the ZnO/MoS₂ heterostructures were investigated using UV-Vis absorption and PL spectroscopies. Figure 4a shows the UV-Vis absorption spectra of the bare ZnO nanorod array (dashed line) and the ZnO/MoS₂ heterostructures. The color change from light to dark colored when the Mo film thickness increases is visible in the optical images shown in the inset. This causes a slight increase in the absorption curves at the visible wavelengths. Because the thickness of the MoS₂ shell around ZnO is very low (few monolayers), only the absorption of ZnO in the UV region (~380 nm) becomes dominant. To observe the fine details of absorption peaks of MoS₂ in the visible region, MoS₂ films were grown on bare FTO glass substrates by sulfurizing pre-deposited Mo thin films with the same nominal thicknesses, i.e., 1.5, 5 and 10 nm. These MoS₂ samples on a bare FTO exhibit two peaks (P_A and P_B) at 675 and 625 nm, as shown in Figure 4b. These

two excitonic peaks correspond to the “A” and “B” transitions between the split maxima of the valence band and the conduction band minimum at the K point of the Brillouin zone [18]. The band near 440 nm, for the sample grown using 1.5 nm of Mo, corresponds to the transition “C” assigned to the van Hove singularities in the electronic density of states [42].

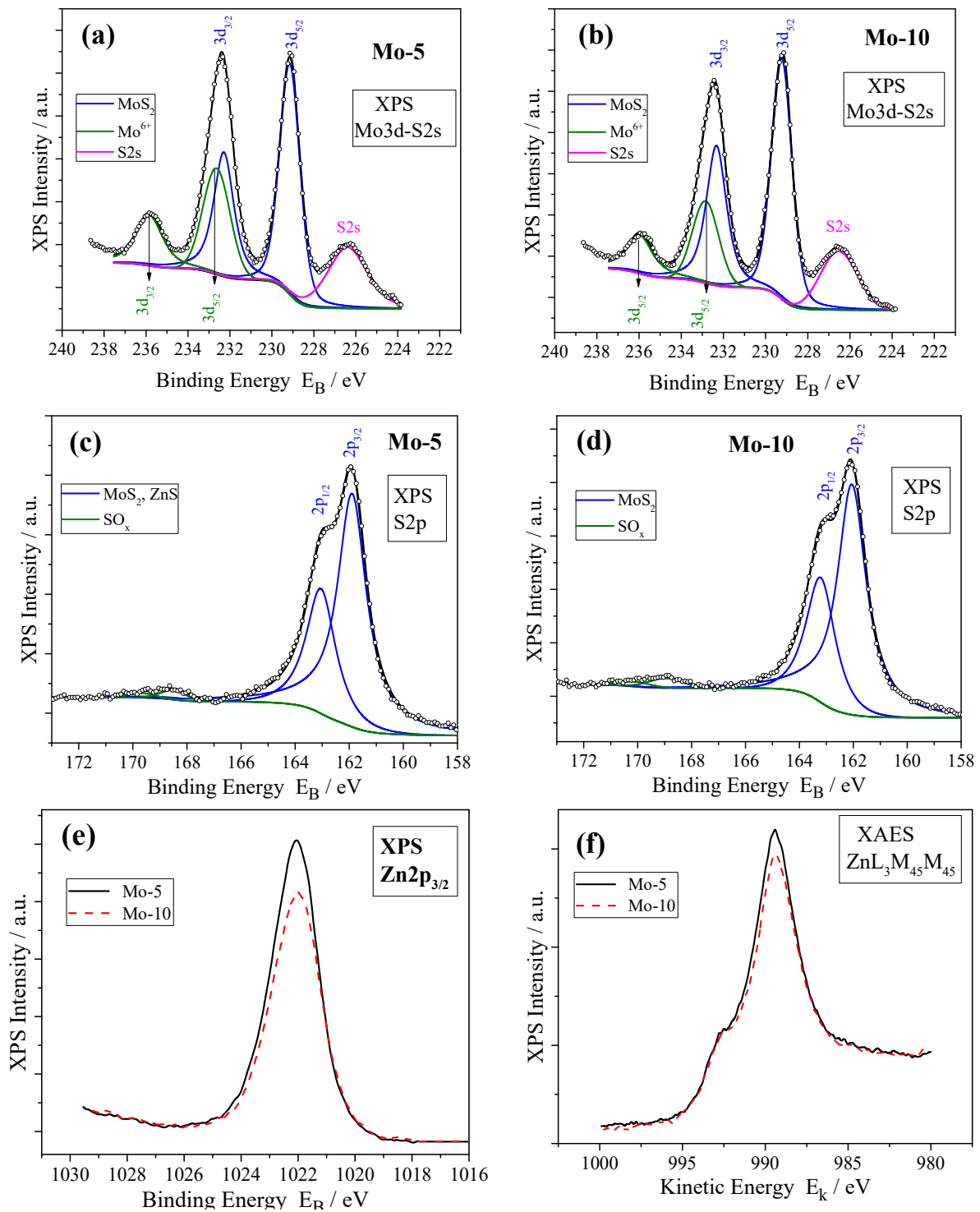


Figure 3. (a,b) Deconvoluted Mo3d XPS peak of Mo-5 and Mo-10 heterostructures. (c,d) Deconvoluted S2p XPS peak of Mo-5 and Mo-10 heterostructures. (e,f) Zn2p_{3/2} spectra and ZnLMM XAES spectra of Mo-5 and Mo-10 heterostructures.

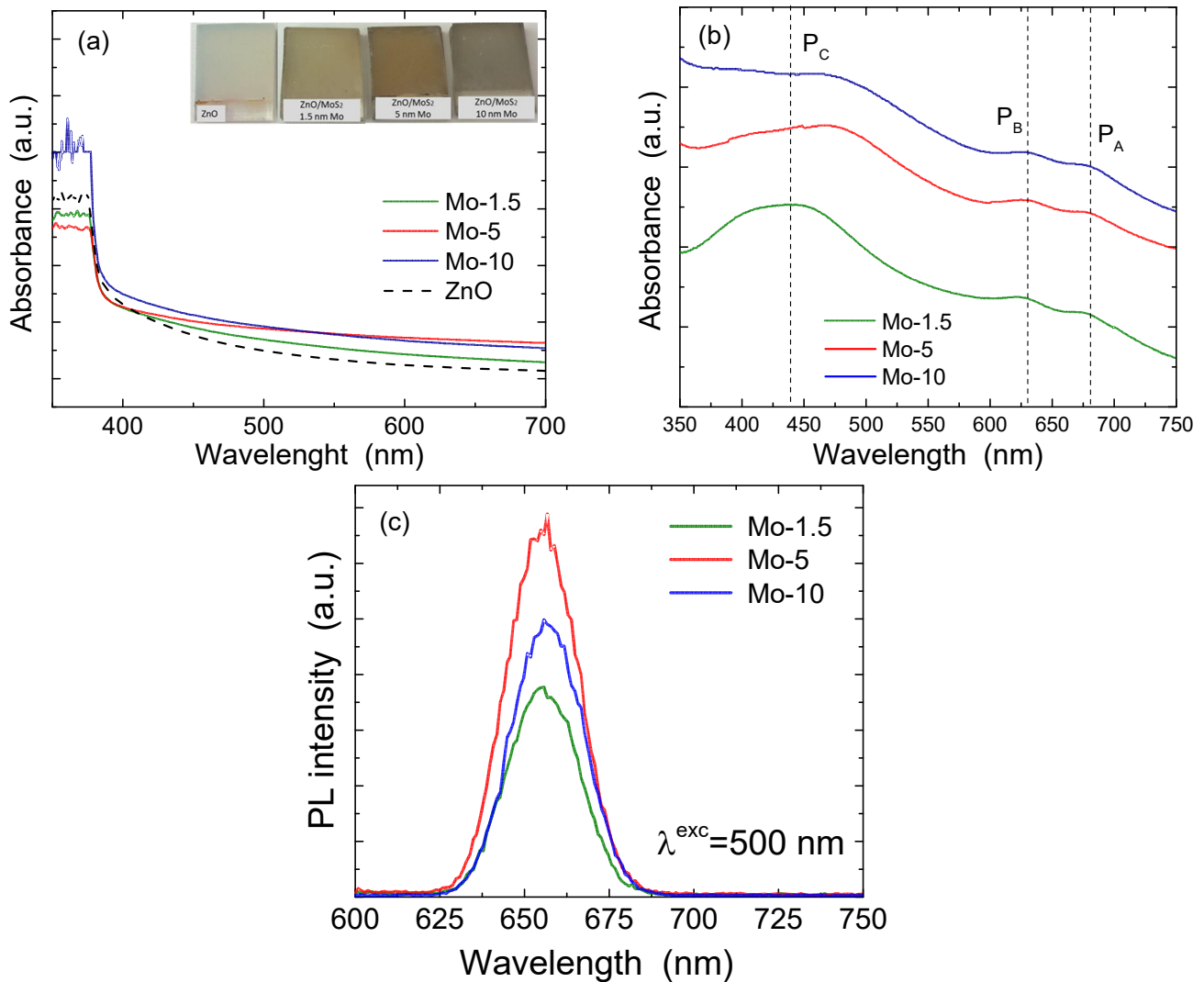


Figure 4. (a) UV-vis absorption spectra of the bare ZnO and ZnO/MoS₂ heterostructures; the inset shows optical images of the samples. (b) Absorption spectra of MoS₂ films deposited on FTO glass substrate. (c) Photoluminescence spectra of ZnO/MoS₂ heterostructures (excitation at 500 nm).

The PL spectra, shown in Figure 4c, were recorded with excitation energy of 500 nm. Since a conventional PL instrument was used, the PL signal arises from a very wide area of about a few mm², hence being representative of the sample homogeneity. For all three heterostructures, the spectra consist of one emission peak at around 655 nm, which is attributed to the direct band gap transitions at the K point of the Brillouin zone. The position of the PL peaks is almost unchanged for the three different heterostructures. In addition, the PL intensity does not substantially increase with decreasing MoS₂ thickness, down to the monolayer. There are two main factors that the current data cannot be directly compared to the literature data. First, as mentioned above, the PL spectra have been acquired in a way that the spot on the sample surface is several mm² averaging a vast number of sites, while most PL data in the literature pertains to micro-PL measurements using laser beam focusing by objectives. Second, the electronic structure of MoS₂ layers grown on ZnO using the current method differs considerably from that of neat MoS₂ films because the ZnO-MoS₂ interface introduces mixed metal oxo-sulfide species, as evidenced by the XPS analysis. Such mixed species are expected to alter the PL properties of neat MoS₂.

3.3.2. Raman Spectroscopy

Raman spectroscopy was employed to study crystallinity and estimate the thickness of the MoS₂ films on ZnO NWs. Representative Raman spectra are shown in Figure 5a, confirming the growth of 2H-MoS₂. A representative full-range Raman spectrum is shown in Figure S2. In all cases, the Raman spectra exhibit two intense bands at ~385 and ~407 cm⁻¹, corresponding to the out-of-plane A_{1g} and in-plane E_{2g}¹ modes, respectively. The first mode results from vibrations of S atoms in opposite directions, while the second mode is associated with the opposite vibration of two S atoms with respect to the Mo atom [19]. Based on the proposed correlation [16,18] between the number of MoS₂ monolayers and the peak frequency difference ($\Delta\omega$) between A_{1g} and E_{2g}¹ modes, the thickness of the MoS₂ sheath was estimated, and it is illustrated in Figure 5b. The solid squares in Figure 5b denote the points of the correlation proposed in [18]. The data of the current work revealed that the difference in $\Delta\omega$ ($= A_{1g} - E_{2g}^1$) increases from 19.5 to 21.6 when the Mo-sputtered film increases from 1.5 to 10 nm. These values correspond to layer thickness of MoS₂ of roughly 1, 2 and (less than) 3 monolayers for the Mo films of 1.5, 5 and 10 nm, respectively. This finding dictates that the preparation method employed in this work can offer to tune the thickness of the MoS₂ sheath layer with monolayer resolution. This is important considering that the optical bandgap energy of MoS₂ strongly depends on the number of layers at the few monolayers limit.

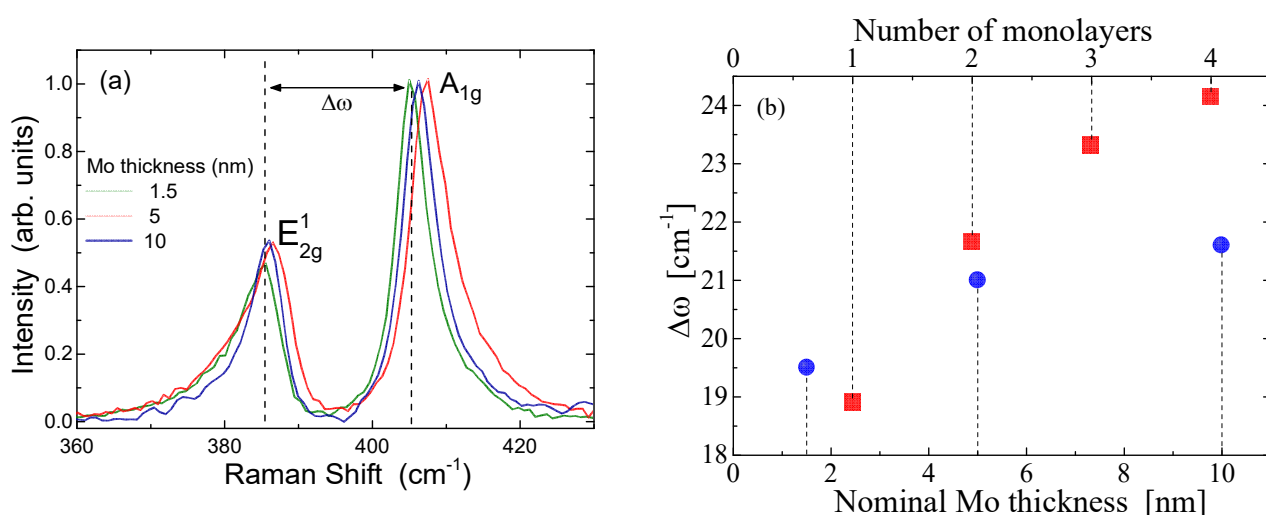


Figure 5. (a) Raman spectra of ZnO/MoS₂ heterostructures. (b) The dependence of $\Delta\omega$ vs. the nominal Mo thickness (solid spheres). The solid squares denote the dependence of $\Delta\omega$ against the number of MoS₂ monolayers taken from Ref. [18].

4. Photoelectrochemical Measurements

To evaluate the PEC activity of the heterostructures, linear sweep voltammetry curves (LSV) were performed both in the dark (dashed lines) and under illumination (solid lines) conditions. LSV curves of bare ZnO and ZnO/MoS₂ heterostructures with a different nominal thickness of Mo are presented in Figure 6a. It is observed that the onset potential of bare ZnO under illumination is comparable with that of the ZnO/MoS₂ structure (Figure 6a). The onset potential for all the ZnO/MoS₂ heterostructures is approximately the same and around 0.15 V vs. RHE. Other studies such as Jian et al. [31] observed an obvious cathodic shift of the onset potential for the ZnO/MoS₂ nanocables morphology in comparison with bare ZnO.

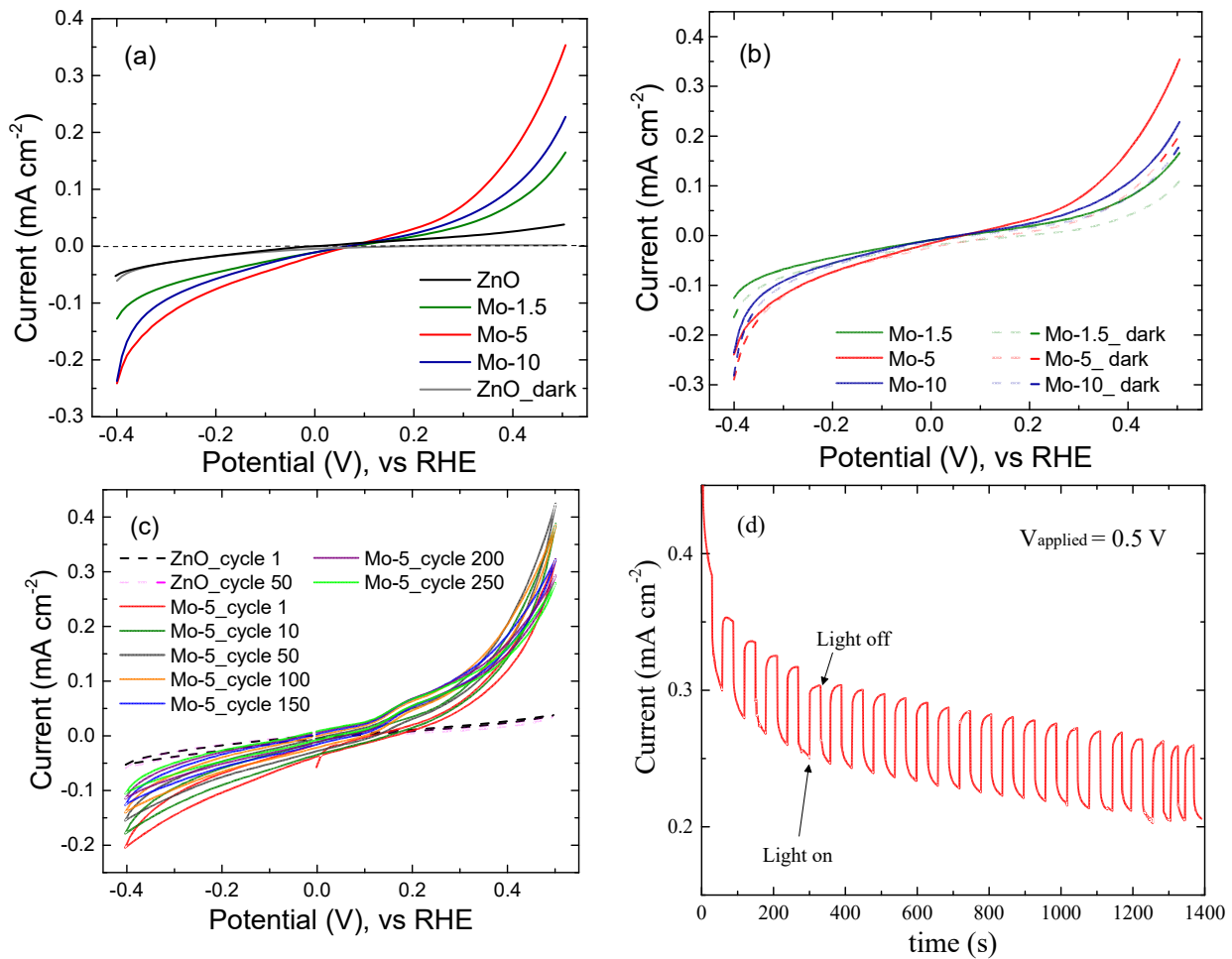


Figure 6. (a,b) LSV curves both in the dark and under illumination of bare ZnO and ZnO/MoS₂ heterostructures with different nominal Mo thicknesses (scan rate 50 mV s⁻¹). (c) Cyclic voltammograms of bare ZnO NWs and ZnO/MoS₂ heterostructures for the Mo-5 sample. (d) Chronoamperometric curve (*J* vs. *t*) for the Mo-5 sample at the applied potential of 0.5 V vs. RHE under chopped illumination.

The photocurrent density is improved for all the ZnO/MoS₂ samples and does not seem to reach the saturation current value up to 0.5 V vs. RHE. The data reveal a non-monotonic dependence of the current vs. the pre-deposited Mo film thickness. In particular, the Mo-5 heterostructures are found to exhibit the best activity towards OER with a photocurrent value equal to 0.35 mA cm⁻² at 0.5 V, which is almost 10 times higher than that of bare ZnO NWs. Further increase in the MoS₂ thickness causes a decrease in the photocurrent density of about 34 % in relation to the maximum value. The layer-dependent electrocatalysis can be correlated to the hopping of electrons in the vertical direction of MoS₂ layers over an interlayer potential barrier, according to Cao et al. [43], who observed that the catalytic activity of MoS₂ deteriorates by a factor of ~4.5 for every additional layer of MoS₂. On the other hand, Trung et al. [33] prepared ZnO/MoS₂ heterostructures with two different thicknesses of Mo, 90 nm and 140 nm, to observe the catalytic dependence from the thickness of MoS₂ layers. They concluded that the thicker sheath of MoS₂ was catalytically more active; however, only by a few %. The non-monotonic dependence of the current density observed in the current investigation calls for a rational explanation, as it is not a trivial finding in relevant studies. Although the reason underlying this effect is still debatable, this non-monotonic behavior could potentially be accounted for in the following context. The change in the photoanode performance (i.e., current density) depends upon two competing factors. One is related to the increase in the thickness (coverage) of the MoS₂ sheath, which causes an increase in the absorbed visible photons. The latter stimulate

charge carrier generation and hence enhanced water splitting. On the other hand, the increase in the deposited Mo metal film indicates that a wider interfacial zone among the two semiconductors is being built up. The latter and the possible presence of traces of unreacted Mo metal at the interfacial zone could be an inhibiting factor for efficient charge separation. The two aforementioned competing factors seem to compromise each other, providing the best performance at the moderate MoS₂ thickness, i.e., the Mo-5 sample.

The value of the ZnO dark current is significantly lower than the photocurrent. As shown in Figure 6a with black and grey lines, respectively. However, in the case of ZnO/MoS₂ heterostructures, the dark current has a measurable value, as depicted in Figure 6b. The dark current indicates that chemical reactions can take place in the interface between the photoanode and the electrolyte in the absence of illumination. In this context, the ZnO/MoS₂ heterostructures also exhibit electrocatalytic behavior. Except for electrocatalysis, the dark current may attribute to electro-corrosion of MoS₂, in which active S atoms can react with redox species in the solution [31].

The stability of the bare ZnO and ZnO/MoS₂ heterostructure with the best catalytic performance (Mo-5 sample) has further been examined by cyclic voltammetry (CV) measurements, as illustrated in Figure 6c. The CV curves are carried out in the range of -0.4 V to 0.5 V vs. RHE under illumination. The anode of the bare ZnO NWs is stable after 50 cycles. The ZnO/MoS₂ sample shows an improved behavior after 10 cycles, while at the 50th cycle, it has its maximum photocurrent value of 0.42 mA cm⁻² at 0.5 V vs. RHE. After the 50th cycle, the photocurrent starts to deteriorate until it reaches the initial value after 150 cycles.

Figure 6d displays the photocurrent response of the Mo-5 sample for several on-off cycles at an applied potential of 0.5 V vs. RHE under chopped illumination. When illumination commences, a sharp increase in the current response is increased, which is attributed to the photogeneration of charged carriers. The current response in the dark does not approach the zero values, indicating that ZnO/MoS₂ heterostructures also exhibit electrocatalytic behavior in accordance with their high values of dark currents, shown in Figure 6b.

The photocurrent of the Mo-5 sample exhibits presents reliable stability up to 1400 s, presumably due to the sacrificial polysulfide electrolyte as Na₂S acts as a hole scavenger. As it has already been reported elsewhere [44,45], this type of electrolyte diminishes photocorrosion of the catalyst's surface, while aqueous electrolytes, such as KOH or Na₂SO₄, lead to surface dissolution. It is worth mentioning that the stability in the current study extends to much longer periods than those reported in previous PEC investigations, i.e., 600 s in [31] and 500 s in [33].

The ZnO/MoS₂ heterostructure is essentially a p-n junction where energy band alignment takes place at the interface. The reactions describing the water-splitting process in the current case are depicted by the reactions (1) to (4). The absorption of photons with energy close or higher than the optical bandgap causes the creation of electron-holes pairs (reaction 1). The electrons transport through the ZnO NWs to the FTO substrate and then are transferred through the external circuit to the Pt counter electrode to induce hydrogen production. The holes travel to the semiconductor/ electrolyte interface and react with S²⁻ ions from the electrolyte molecules to form S₂²⁻ (reaction 2). The SO₃²⁻ ions from Na₂SO₃ reduce S₂²⁻ to S²⁻ (reaction 3), and they can react with S²⁻ to generate S₂O₃²⁻ (reaction 4) to prevent sulfur deposition.



Figure 7 illustrates the separation and transport processes of the photoinduced charge carriers in the photoelectrochemical water splitting process over the ZnO/MoS₂ heterostructure.

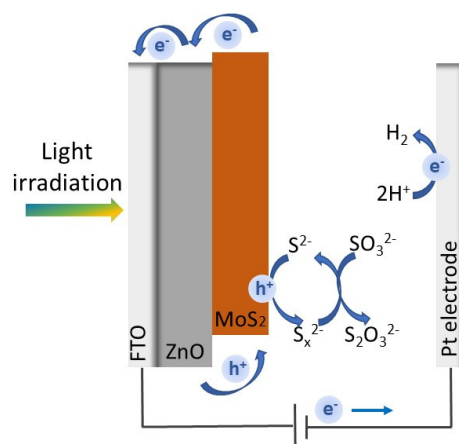


Figure 7. A schematic of the charge carriers' reactions in a PEC splitting cell.

5. Conclusions

In summary, well-aligned ZnO/MoS₂ core/sheath heterostructures have been grown on FTO/glass substrate by a sequence of synthesis methods, comprising chemical bath deposition of the ZnO nanowire arrays and Mo sputtering followed by low-temperature sulfurization. The current approach offers control over the final thickness of the MoS₂ layer grown on ZnO. Electron microscopy and spectroscopic techniques have provided information on the morphology, thickness and details of the interface between the two semiconductors, i.e., ZnO and MoS₂. It has been found that the Mo thin films thickness, which is pre-deposited on ZnO NWs surface, determines the MoS₂ thickness under particular growth (sulfurization) conditions. XPS measurements have revealed a variety of chemical species beyond the ZnO and MoS₂. In particular, the current work provides evidence about a non-abrupt interface between the two semiconductors. The composition of the interface changes gradually from the core towards the shell in the following sequence ZnO → ZnO_yS_{1-y} and/or ZnS → MoO_{3-x}S_x → MoS₂. PEC measurements have shown a clear improvement of the photocurrent for all heterostructures in comparison to the neat ZnO NW arrays and a very good long-term stability. The heterostructures prepared with sulfurization of Mo film with a nominal thickness of ca. 5 nm have shown the best photocurrent and enhanced stability.

Supplementary Materials: The following are available online at <https://www.mdpi.com/article/10.3390/applnano2030012/s1>, Figure S1: XPS survey scans, Figure S2: Raman spectrum.

Author Contributions: Conceptualization, S.N.Y. and S.G.N.; methodology, K.G., A.A. and L.S.; investigation, K.G., A.A. and L.S.; writing—original draft preparation, K.G., A.A., L.S., S.G.N. and S.N.Y.; writing—review and editing, K.G. and S.N.Y.; supervision, S.N.Y. and S.G.N.; funding acquisition, S.N.Y. and S.G.N.; All authors have read and agreed to the published version of the manuscript.

Funding: This research is co-financed by Greece and the European Union (European Social Fund-ESF) through the Operational Programme “Human Resources Development, Education and Lifelong Learning 2014–2020” in the context of the project Photo-electrochemical water splitting with combination of 1-D and 2-D structures” (MIS 5047755).

Institutional Review Board Statement: Not applicable.

Informed Consent Statement: Not applicable.

Data Availability Statement: Not applicable.

Acknowledgments: The authors wish to thank FORTH/ICE-HT for providing experimental facilities and Mary Kollia (Laboratory of Electron Microscopy and Microanalysis, School of Natural Sciences, University of Patras) for the TEM images.

Conflicts of Interest: The authors declare no conflict of interest.

References

1. Ni, M.; Leung, M.K.H.; Leung, D.Y.C.; Sumathy, K. A review and recent developments in photocatalytic water-splitting using TiO₂ for hydrogen production. *Renew. Sustain. Energy Rev.* **2007**, *11*, 401–425. [[CrossRef](#)]
2. Nowotny, J.; Bak, T.; Nowotny, M.K.; Sheppard, L.R. Titanium dioxide for solar-hydrogen I. Functional properties. *Int. J. Hydrogen Energy* **2007**, *32*, 2609–2629. [[CrossRef](#)]
3. Fujishima, A.; Zhang, X.; Tryk, D.A. TiO₂ photocatalysis and related surface phenomena. *Surf. Sci. Rep.* **2008**, *63*, 515–582. [[CrossRef](#)]
4. Wolcott, A.; Smith, W.A.; Kuykendall, T.R.; Zhao, Y.; Zhang, J.Z. Photoelectrochemical Study of Nanostructured ZnO Thin Films for Hydrogen Generation from Water Splitting. *Adv. Funct. Mater.* **2009**, *19*, 1849–1856. [[CrossRef](#)]
5. Shet, S. Zinc Oxide (ZnO) Nanostructures for Photoelectrochemical Water Splitting Application. *ECS Trans.* **2007**, *33*, 15–25. [[CrossRef](#)]
6. Nguyen, D.-T.; Shin, E.-C.; Cho, D.-C.; Chae, K.-W.; Lee, J.-S. Photoelectrochemical performance of ZnO thin film anodes prepared by solution method. *Int. J. Hydrogen Energy* **2014**, *39*, 20764–20770. [[CrossRef](#)]
7. Santato, C.; Ulmann, M.; Augustynski, J. Enhanced Visible Light Conversion Efficiency Using Nanocrystalline WO₃ Films. *Adv. Mater.* **2001**, *13*, 511–514. [[CrossRef](#)]
8. Seabold, J.A.; Choi, K.S. Effect of a cobalt-based oxygen evolution catalyst on the stability and the selectivity of photo-oxidation reactions of a WO₃ photoanode. *Chem. Mater.* **2011**, *23*, 1105–1112. [[CrossRef](#)]
9. Wang, Z.L. ZnO nanowire and nanobelt platform for nanotechnology. *Mater. Sci. Eng. R Rep.* **2009**, *64*, 33–71. [[CrossRef](#)]
10. Wang, Z.L. Zinc oxide nanostructures: Growth, properties and applications. *J. Phys. Condens. Matter* **2004**, *16*, R829–R858. [[CrossRef](#)]
11. Tamirat, A.G.; Rick, J.; Dubale, A.A.; Su, W.-N.; Hwang, B.-J. Using hematite for photoelectrochemical water splitting: A review of current progress and challenges. *Nanoscale Horiz.* **2016**, *1*, 243–267. [[CrossRef](#)]
12. Kim, T.W.; Choi, K.-S. Nanoporous BiVO₄ Photoanodes with Dual-Layer Oxygen Evolution Catalysts for Solar Water Splitting. *Science* **2014**, *343*, 990–994. [[CrossRef](#)]
13. Wang, L.; Tian, G.; Chen, Y.; Xiao, Y.; Fu, H. In situ formation of a ZnO/ZnSe nanonail array as a photoelectrode for enhanced photoelectrochemical water oxidation performance. *Nanoscale* **2016**. [[CrossRef](#)] [[PubMed](#)]
14. Cho, S.; Jang, J.-W.; Lim, S.-H.; Kang, H.J.; Rhee, S.-W.; Lee, J.S.; Lee, K.-H. Solution-based fabrication of ZnO/ZnSe heterostructure nanowire arrays for solar energy conversion. *J. Mater. Chem.* **2011**, *21*, 17816. [[CrossRef](#)]
15. Xu, H.; Mo, R.; Cheng, C.; Ai, G.; Chen, Q.; Yang, S.; Li, H.; Zhong, J. ZnSe/CdS/CdSe triple-sensitized ZnO nanowire arrays for multi-bandgap photoelectrochemical hydrogen generation. *RSC Adv.* **2014**, *4*, 47429–47435. [[CrossRef](#)]
16. Ouyang, W.X.; Yu, Y.X.; Zhang, W. De High and stable photoelectrochemical activity of ZnO/ZnSe/CdSe/Cu_xS core-shell nanowire arrays: Nanoporous surface with Cu_xS as a hole mediator. *Phys. Chem. Chem. Phys.* **2015**, *17*, 14827–14835. [[CrossRef](#)]
17. Chen, Y.; Wang, L.; Wang, W.; Cao, M. Enhanced photoelectrochemical properties of ZnO/ZnSe/CdSe/Cu_{2-x}Se core-shell nanowire arrays fabricated by ion-replacement method. *Appl. Catal. B Environ.* **2017**, *209*, 110–117. [[CrossRef](#)]
18. Lee, C.; Yan, H.; Brus, L.E.; Heinz, T.F.; Hone, K.J.; Ryu, S. Anomalous Lattice Vibrations of Single and Few-Layer MoS₂. *ACS Nano* **2010**, *4*, 2695–2700. [[CrossRef](#)]
19. Li, H.; Zhang, Q.; Yap, C.C.R.; Tay, B.K.; Edwin, T.H.T.; Olivier, A.; Baillargeat, D. From Bulk to Monolayer MoS₂: Evolution of Raman Scattering. *Adv. Funct. Mater.* **2012**, *22*, 1385–1390. [[CrossRef](#)]
20. Mak, K.F.; Lee, C.; Hone, J.; Shan, J.; Heinz, T.F. Atomically thin MoS₂: A new direct-gap semiconductor. *Phys. Rev. Lett.* **2010**, *105*, 2–5. [[CrossRef](#)] [[PubMed](#)]
21. Kang, K.; Xie, S.; Huang, L.; Han, Y.; Huang, P.Y.; Mak, K.F.; Kim, C.-J.; Muller, D.; Park, J. High-mobility three-atom-thick semiconducting films with wafer-scale homogeneity. *Nature* **2015**, *520*, 656–660. [[CrossRef](#)] [[PubMed](#)]
22. Salmeron, M.; Somorjai, G.A.; Wold, A.; Chianelli, R.; Liang, K.S. The adsorption and binding of thiophene, butene and H₂S on the basal plane of MoS₂ single crystals. *Chem. Phys. Lett.* **1982**, *90*, 105–107. [[CrossRef](#)]
23. Helveg, S.; Lauritsen, J.V.; Lægsgaard, E.; Stensgaard, I.; Nørskov, J.K.; Clausen, B.S.; Topsøe, H.; Besenbacher, F. Atomic-Scale Structure of Single-Layer MoS₂ Nanoclusters. *Phys. Rev. Lett.* **2000**, *84*, 951–954. [[CrossRef](#)]
24. Jaramillo, T.F.; Jorgensen, K.P.; Bonde, J.; Nielsen, J.H.; Horch, S.; Chorkendorff, I. Identification of Active Edge Sites for Electrochemical H₂ Evolution from MoS₂ Nanocatalysts. *Science* **2007**, *317*, 100–102. [[CrossRef](#)] [[PubMed](#)]
25. Yuan, Y.-J.; Wang, F.; Hu, B.; Lu, H.-W.; Yu, Z.-T.; Zou, Z.-G. Significant enhancement in photocatalytic hydrogen evolution from water using a MoS₂ nanosheet-coated ZnO heterostructure photocatalyst. *Dalton Trans.* **2015**, *44*, 10997–11003. [[CrossRef](#)]
26. Lee, Y.H.; Zhang, X.Q.; Zhang, W.; Chang, M.T.; Lin, C.T.; Di Chang, K.; Yu, Y.C.; Wang, J.T.W.; Chang, C.S.; Li, L.J.; et al. Synthesis of large-area MoS₂ atomic layers with chemical vapor deposition. *Adv. Mater.* **2012**, *24*, 2320–2325. [[CrossRef](#)]
27. Chhowalla, M.; Shin, H.S.; Eda, G.; Li, L.-J.; Loh, K.P.; Zhang, H. The chemistry of two-dimensional layered transition metal dichalcogenide nanosheets. *Nat. Chem.* **2013**, *5*, 263–275. [[CrossRef](#)]

28. Zhan, G.; Zhang, J.; Wang, Y.; Yu, C.; Wu, J.; Cui, J.; Shu, X.; Qin, Y.; Zheng, H.; Sun, J.; et al. MoS₂ quantum dots decorated ultrathin NiO nanosheets for overall water splitting. *J. Colloid Interface Sci.* **2020**, *566*, 411–418. [[CrossRef](#)] [[PubMed](#)]
29. Xiong, D.; Zhang, Q.; Li, W.; Li, J.; Fu, X.; Cerqueira, M.F.; Alpuim, P.; Liu, L. Atomic-layer-deposited ultrafine MoS₂ nanocrystals on cobalt foam for efficient and stable electrochemical oxygen evolution. *Nanoscale* **2017**, *9*, 2711–2717. [[CrossRef](#)]
30. Li, Y.; Wang, H.; Xie, L.; Liang, Y.; Hong, G.; Dai, H. MoS₂ Nanoparticles Grown on Graphene: An Advanced Catalyst for the Hydrogen Evolution Reaction. *J. Am. Chem. Soc.* **2011**, *133*, 7296–7299. [[CrossRef](#)]
31. Jian, W.; Cheng, X.; Huang, Y.; You, Y.; Zhou, R.; Sun, T.; Xu, J. Arrays of ZnO/MoS₂ nanocables and MoS₂ nanotubes with phase engineering for bifunctional photoelectrochemical and electrochemical water splitting. *Chem. Eng. J.* **2017**, *328*, 474–483. [[CrossRef](#)]
32. Kwon, I.S.; Debela, T.T.; Kwak, I.H.; Park, Y.C.; Seo, J.; Shim, J.Y.; Yoo, S.J.; Kim, J.G.; Park, J.; Kang, H.S. Ruthenium Nanoparticles on Cobalt-Doped 1T' Phase MoS₂ Nanosheets for Overall Water Splitting. *Small* **2020**, *16*, 1–10. [[CrossRef](#)] [[PubMed](#)]
33. Trung, T.N.; Seo, D.B.; Quang, N.D.; Kim, D.; Kim, E.T. Enhanced photoelectrochemical activity in the heterostructure of vertically aligned few-layer MoS₂ flakes on ZnO. *Electrochim. Acta* **2018**, *260*, 150–156. [[CrossRef](#)]
34. Mohanty, B.; Ghorbani-Asl, M.; Kretschmer, S.; Ghosh, A.; Guha, P.; Panda, S.K.; Jena, B.; Krasheninnikov, A.V.; Jena, B.K. MoS₂ Quantum Dots as Efficient Catalyst Materials for the Oxygen Evolution Reaction. *ACS Catal.* **2018**, *8*, 1683–1689. [[CrossRef](#)]
35. Laursen, A.B.; Kegnæs, S.; Dahl, S.; Chorkendorff, I. Molybdenum sulfides—Efficient and viable materials for electro- and photoelectrocatalytic hydrogen evolution. *Energy Environ. Sci.* **2012**, *5*, 5577. [[CrossRef](#)]
36. Koper, M.T.M. Thermodynamic theory of multi-electron transfer reactions: Implications for electrocatalysis. *J. Electroanal. Chem.* **2011**, *660*, 254–260. [[CrossRef](#)]
37. Govatsi, K.; Seferlis, A.; Neophytides, S.G.; Yannopoulos, S.N. Influence of the morphology of ZnO nanowires on the photoelectrochemical water splitting efficiency. *Int. J. Hydrogen Energy* **2018**, *43*, 4866–4879. [[CrossRef](#)]
38. Sygellou, L. An in-situ photoelectron spectroscopy study of the thermal processing of ammonium tetrathiomolybdate, (NH₄)₂MoS₄, precursor. *Appl. Surf. Sci.* **2019**, *476*, 1079–1085. [[CrossRef](#)]
39. Wang, H.; Lu, Z.; Kong, D.; Sun, J.; Hymel, T.M.; Cui, Y. Electrochemical Tuning of MoS₂ Nanoparticles on Three-Dimensional Substrate for Efficient Hydrogen Evolution. *ACS Nano* **2014**, *8*, 4940–4947. [[CrossRef](#)]
40. Barreca, D.; Gasparotto, A.; Maragno, C.; Tondello, E.; Spalding, T.R. Analysis of Nanocrystalline ZnS Thin Films by XPS. *Surf. Sci. Spectra* **2002**, *9*, 54–61. [[CrossRef](#)]
41. Siow, K.S.; Britcher, L.; Kumar, S.; Griesser, H.J. Sulfonated Surfaces by Sulfur Dioxide Plasma Surface Treatment of Plasma Polymer Films. *Plasma Process. Polym.* **2009**, *6*, 583–592. [[CrossRef](#)]
42. Britnell, L.; Ribeiro, R.M.; Eckmann, A.; Jalil, R.; Belle, B.D.; Mishchenko, A.; Kim, Y.-J.; Gorbachev, R.V.; Georgiou, T.; Morozov, S.V.; et al. Strong Light-Matter Interactions in Heterostructures of Atomically Thin Films. *Science* **2013**, *340*, 1311–1314. [[CrossRef](#)] [[PubMed](#)]
43. Cao, L.; Yu, Y.; Huang, S.; Li, Y.; Steinmann, S.N.; Yang, W. Layer-dependent Electrocatalysis of MoS₂ for Hydrogen Evolution. *Nano Lett.* **2014**, *14*, 553–558.
44. Sánchez-Tovar, R.; Fernández-Domene, R.M.; Montañés, M.T.; Sanz-Marco, A.; Garcia-Antón, J. ZnO/ZnS heterostructures for hydrogen production by photoelectrochemical water splitting. *RSC Adv.* **2016**, *6*, 30425–30435. [[CrossRef](#)]
45. Kushwaha, A.; Aslam, M. ZnS shielded ZnO nanowire photoanodes for efficient water splitting. *Electrochim. Acta* **2014**, *130*, 222–231. [[CrossRef](#)]